JOURNAL OF HYDRAULIC RESEARCH
2024, VOL. 62, NO. 5, 461–475
https://doi.org/10.1080/00221686.2024.2401903

IAHR AIRH International Association for Hydro-Environment Engineering and Research
Hosted by Spain Water and IWHR, China

Taylor & Francis
Taylor & Francis Group

RESEARCH PAPER

Check for updates

Breaching of sand dikes: assessment of 1D and 2D numerical models against laboratory experiments

Nathan Delpierre[a], Fabian Franzini[b], Pierre-Yves Gousenbourger[c], Sylvie Van Emelen[d], Yves Zech[e] and Sandra Soares-Frazao [f]

[a]Institute of Mechanics, Materials and Civil Engineering, UCLouvain, Louvain-la-Neuve, Belgium; [b]Institute of Mechanics, Materials and Civil Engineering, UCLouvain, Louvain-la-Neuve, Belgium and Fonds National de la Recherche Scientifique, Bruxelles, Belgium; [c]Reasearcher at Institute of Mechanics, Materials and Civil Engineering, UCLouvain, Louvain-la-Neuve, Belgium; [d]Unité Génie Construction et Géomètre, Haute Ecole Léonard de Vinci, Bruxelles, Belgium; [e]Institute of Mechanics, Materials and Civil Engineering, UCLouvain, Louvain-la-Neuve, Belgium; [f]Institute of Mechanics, Materials and Civil Engineering, UCLouvain, Louvain-la-Neuve, Belgium

ABSTRACT

Dike failures often induce highly damaging floods. Improved understanding of the inherent mechanisms is important to predict and prevent dike failures. This research focuses on sand dike failure by overtopping. During the experiments, the evolution of nine sections was monitored using laser-sheet while the water level in the upstream reservoir was captured using ultrasonic gauges. The impact of the grain size was studied by comparing a fine and a coarser sand. Even though the failure mechanisms look similar in both cases, some differences could be observed in the evolution of the geometry of the dike. Finally, the failure was simulated with 1D and 2D models. The 1D model shows good results for the initial stage of the dike evolution and in predicting the evolution of the width of the breach. The 2D model predicts the morphological evolution of the dike more accurately but slightly overestimates the widening of the breach.

ARTICLE HISTORY
Received 22 September 2023
Accepted 3 September 2024

KEYWORDS
Dike failure; erosion processes; laboratory studies; laser sheet; one-dimensional models; two-dimensional models

1. Introduction

Dikes, or earthen embankments, play a key role in flood defence but also in water resource management or energy production. In areas such as the north of Belgium and the Netherlands, millions of people are living under the current sea-level. They are thus greatly dependent on the proper functioning of these structures. For the Netherlands only, a 22,000 km long network of dikes has been developed, while the country only counts 880 km of coastline.

Therefore, dike failures can greatly worsen flood events as they induce important flows in areas intended to be protected. Overtopping is the most common failure mechanism for earthen embankments, representing 34% of cases (Foster et al., 2000). Examples include the Hurricane Katrina in New Orleans (2005), where all dike failures were observed with overtopping (Sills et al., 2008), but also the floods that occurred in 2013 along the Elbe River causing multiple failures.

In such scenarios, it is crucial for decision makers to gain a better knowledge of the remaining time before the dike will break and of the volume of water that will pass through it once water begins to overflow the dike. This information can be utilized as an input hydrograph to facilitate the creation of accurate and coherent flood maps.

The present research focuses on the failure of non-cohesive sandy dikes made of uniform material by overtopping. This type of failure has been studied extensively over the last decades as non-cohesive fill dikes are the most sensitives to surface erosion. Indeed, Morris et al. (2009) point out that the failure is mostly led by progressive surface erosion for non-cohesive fill material. Visser (1998) first described the failure process for fine sand dikes by clearly identifying the different steps of the breach widening. His theory highlights the cohesive behaviour of fine sand that is not always representative of non-cohesive material. On the other hand, Coleman et al. (2002) extended the study to coarse non-cohesive sand dikes and highlighted the presence of a pivot point, around which the dike rotates while being eroded. These theories have been further enhanced by Zhang et al. (2017) and Zhou et al. (2019). Experiments usually focus on the influence of several parameters, such as the sediment nature, dike height and discharge (Schmocker & Hager, 2012), the grain size distribution (Schmocker et al., 2014), the shape and headwater elevation (Müller et al., 2016) or the material constituting an eventual pavement (Pan et al., 2015; Zhang et al., 2017).

As regards numerical simulations, the complexity of the ongoing physical processes and the associated

CONTACT Sandra Soares-Frazao sandra.soares-frazao@uclouvain.be

variability make it difficult to model dike breaching in a comprehensive way. Therefore, many authors still rely on parametric breach models using regression equations to estimate the evolution of the failure mechanism (ASCE/EWRI Task Committee on Dam/Levee Breaching, 2011). Based on multiple case studies, laws describing relations between the overtopping flows and some physical parameters, like the breach width or water inflow, can be derived. Other approaches can be seen as semi-physical as they try to incorporate the geometry of the breach, considered as a rectangle or trapezoidal forms, and to describe its evolution in time considering some simplifications (ASCE/EWRI Task Committee on Dam/Levee Breaching, 2011).

Nevertheless, numerical models are very powerful tools to run predictive simulations. When models are validated by experiments, they can be used to predict behaviour in real life and hence prevent damage or hazard. Many numerical models have now been developed to assess the risk of failure for dikes submitted to overtopping flows with attempts to fully solve the physical process. Based on the idea that the breaching process is mostly dominated by erosion for non-cohesive dikes, most of the models consist in solving the shallow water equations combined with the Exner equation. These models build on specific transport laws and the resolution schemes assume equilibrium bedload transport conditions. That is, the transport rate instantaneously adapts to local flow specifications (see e.g. Wu et al., 2012, Juez et al., 2014, Barzgaran et al., 2019, Meurice & Soares-Frazão, 2020). Recent works consider non-equilibrium bedload transport for dam breaching (Martínez-Aranda et al., 2023). They account for temporal and spatial delay of the sediment transport rate influenced by the flow capacity. Martínez-Aranda et al. (2021) made a specific comparison between equilibrium and non-equilibrium conditions and showed that, under appropriate calibration of the parameters, the non-equilibrium approach performed better in highly transient zones.

In such models, the difficulties in properly describing the process lie mainly in the variability of the material, such as mean grain diameter, compaction or water content. Many transport laws have been developed with a particular range of applications, making this choice critical for the quality of the simulation, as highlighted by Van Emelen et al. (2015). Note that the literature provides mostly closure equations for non-cohesive sands. This is an acceptable approach as soon as the dike is made of sand coarse enough to be considered as non-cohesive. However, humidity confers cohesion and may strongly alter the results. Further work should focus on considering the saturation of water *inside* the dike, as initiated in Delpierre et al. (2023).

This work has two goals. First, we provide a new 1:1 experimental benchmark to the community, with results of dike breaching by overtopping obtained with coarse and fine uniform sands. From the experimental side, an important and interesting development is the extensive use of the laser light sheets, already developed in prior works (Soares-Frazão et al., 2007), to precisely catch the morphological evolution of the breach in time and therefore to provide valuable data for numerical model validation. In addition to the high quality of the measured data, all the parameters required by modellers are provided. Another interesting aspect of the experimental results is the comparison between the behaviours of coarse and fine sand. The results show that the cohesive behaviour of fine sand leads to a higher peak discharge following lateral block failure. The described processes show interesting concordances with the observations of Coleman et al. (2002) and Visser (1998), which allow the dataset to be validated.

Secondly, we compare this benchmark to one-dimensional and two-dimensional finite volume models based on the shallow-water-Exner equations augmented with a bank-failure operator. We show that the one-dimensional simulation, although less accurate and physically less appropriate, provides acceptable results while using significantly less simulation time, and is thus a good quick first estimation. The two-dimensional model used in this paper also solves the shallow-water and Exner equations and is enhanced with a feature first presented by Swartenbroekx et al. (2010) as a bank-failure operator. This feature allows a maximal slope angle to be considered for non-cohesive sand and therefore to correctly represent the local mass failures. The one-dimensional model considers the morphological evolution of arbitrary cross section based on an augmented Roe approach (Franzini & Soares-Frazão, 2018).

The current paper is divided in five sections. Section 2 describes the experimental setup built to run the experiments in the laboratory. Section 3 describes the measurement techniques to capture the bed level evolution and the water evolution in time. Section 4 comments the experimental results concerning the breaching process and the evolution of the captured bed level at the different sections of measure. As this paper is about experimental and numerical modelling, Section 5 describes the numerical one-dimensional and two-dimensional models, whose results will be compared with the experimental results in Section 6. Section 7 is dedicated to the conclusions.

2. Experimental setup

The breaching experiments were carried out at the Hydraulics Laboratory of the Institute of Mechanics, Materials and Civil Engineering (iMMC) of UCLouvain (Belgium). The set-up is illustrated in Figure 1 and consists of a full-scale dike constructed with an initial pilot breach. The flume is 12 m long, 1.2 m wide and 0.32 m high. A pump supplies water to a 2-m long,

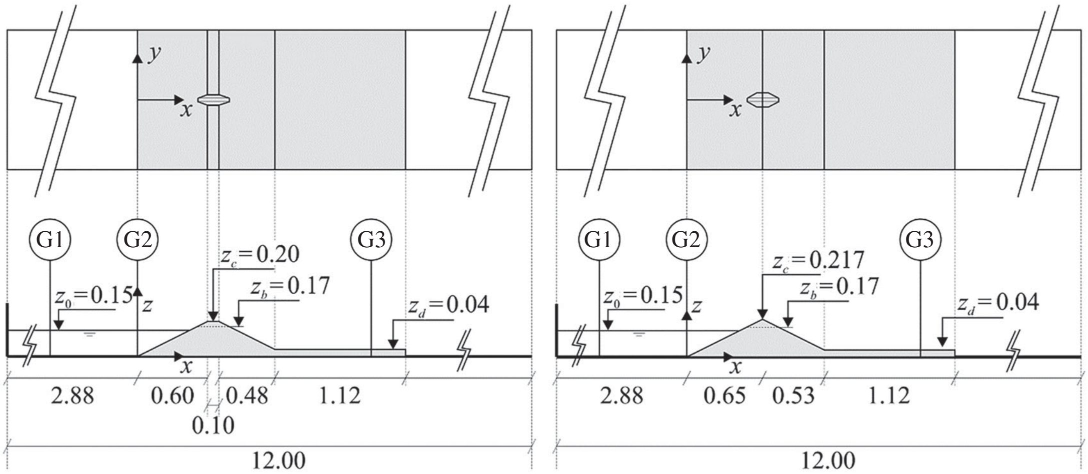

Figure 1. Experimental setup and dimensions of the dike made of (a) coarse sand and (b) fine sand. The only difference relies on the top of the dike. Distances are in metres.

upstream reservoir. The dike is built 2.88 m downstream from the reservoir.

Two dikes were built: one with coarse sand and one with fine sand. Coarse sand has median diameter $d_{50} = 1.7$ mm, and bed porosity $\epsilon_0 = 45\%$ after compaction. Fine sand has median diameter $d_{50} = 0.71$ mm, and bed porosity $\epsilon_0 = 44\%$ after compaction. Both sands have a specific gravity $s = 2.615$. According to widely used formulas, the Manning friction coefficient should range from $0.014\,\mathrm{s\ m^{-1/3}}$ to $0.0167\,\mathrm{s\ m^{-1/3}}$. Finally, the friction coefficient, $n = 0.0167\,\mathrm{s\,m^{-1/3}}$, was determined from uniform flow experiments and chosen for both sands. A dry friction angle of 85° and a wet friction angle of 30° were considered following Swartenbroekx et al. (2010).

Geometrically, the dikes are 1.3 m long and use the whole flume width (1.2 m) with 1:3 slopes, upstream and downstream. Note that the dike made with coarse sand has a crest of 0.1 m length while the dike made with fine sand has no crest for mechanical reasons. An initial trapezoidal breach is dug in each dike to initiate the failure process. The breach has a base width of 0.03 m with a 1:1 slope, and a sand level of 0.17 m at its centre. A sand layer of 1 m long and 0.04 m height is set at the downstream toe of the dike to avoid piping effects.

The upstream part of the dike is initially filled with 0.15 m of water. When the experiment starts, the pump is activated to provide a constant discharge of $4\ \mathrm{l\ s^{-1}}$. This discharge is kept constant during the whole experiment.

3. Measurement techniques

The important parameters studied in the experiments are the water and bed level evolution. These are captured using two types of measurement techniques: ultrasonic probes and laser-sheet. These two techniques have the advantage of being non-intrusive. This prevents any local influence of the measurement on the experiment.

Three ultrasonic probes are used to determine the water level evolution at three locations as illustrated in : just downstream of the reservoir ($x = -\ 0.75$ m), at the upstream toe of the dike ($x = 0$ m) and on the downstream sand layer ($x = 2.05$ m).

The bed level evolution is captured at nine different positions thanks to three laser-sheets (Soares-Frazão et al. 2007), as represented in Figure 2. The experiments are run in a completely dark environment: the bed level is then lit by the laser-sheets, which creates a thin visible red line. The red lines are captured by a camera, as illustrated in Figure 2. We assume that the impact of refraction is negligible given that the camera is placed in front of the dike (Soares-Frazao et al, 2007). This effect is further limited as the water depth over the dike is very small.

The bed profiles are extracted from the pictures using Matlab preprocessing. First, the pictures are orthorectified to remove deformations due to the camera lenses and position. Two deformations can occur (see Figure 3 for a clear example on a chessboard): barrel distortion (b) and perspective distortion (c). Secondly, the bed level lines are isolated, selecting the pixels with the highest contrast. Finally, the results are scaled using the ratio pixel/cm.

To avoid noisy effects due to the proximity of two consecutive lasers, we decided to acquire the bed level at only three positions by trial. The lasers are shifted after each trial in order to multiply the measurements: three trials are hence needed in order to obtain the nine measurements (see Table 1 for the nine positions and their associated trial). Therefore, the repeatability of the data acquisition protocol is crucial to assess the validity of the measurements of the bed level evolution from one trial to another. Here, the validity has been assessed by performing three experiments where the dike was

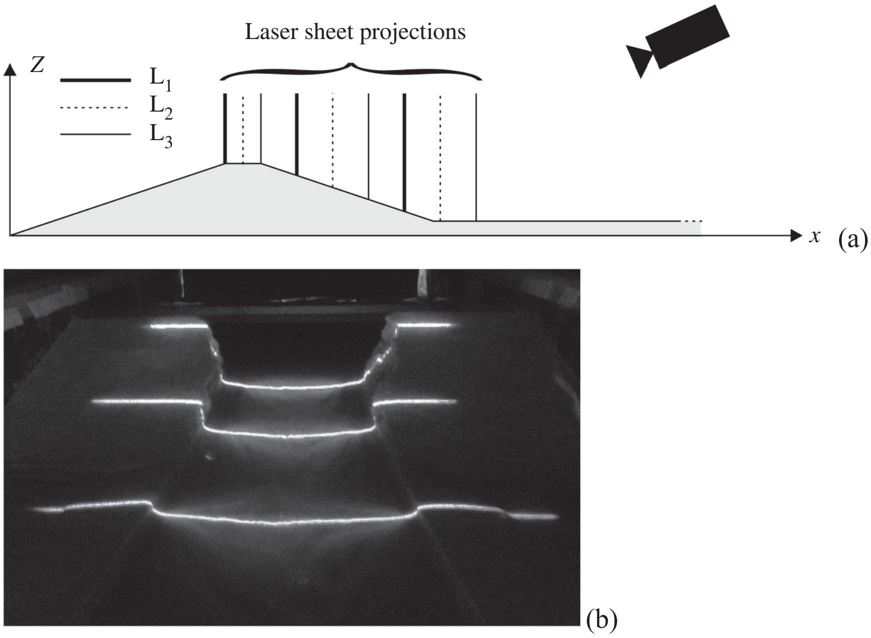

Figure 2. Laser-sheet and camera measurements: (a) indication of the three series of measurements per test (see Table 1 for the exact positions), (b) result for one series of measurements: the laser appears as a white line.

flush by water. During each experiment, we measured the bed level at three different locations. We then compared the results in Figure 4. The experiments were performed with fine sand and coarse sand (for a total of six trials). The results show visually strong similarities and enhance the confidence in the repeatability of the protocol.

4. Results

This section presents the results from the experiments. It is divided in three parts. First, the general process of failure is presented. Second, the breach evolution is studied more closely. Third, the breach discharge is estimated using data on geometry and water level evolution. It is shown, in this section, that the data recorded during this experiment respects the expectations and follows the well-known models of Visser (1998) and Coleman et al. (2002). Therefore, the dataset can be considered as valid and is shared to the community as a new benchmark to study the breaching and the failure of sand dikes.

4.1. Breaching process

The failure mechanism observed for both types of sand confirms the three first stages of dike erosion observed by Visser (1998, §2). Figures 5 (coarse sand) and 6 (fine sand) show pictures of those stages appearing in the present experiments.

In stage I, we observe a steepening of the breach slopes until a critical angle is reached at $t = t_1$. This critical angle is reached at $t_1 = 22$ s for coarse sand and $t_1 = 27$ s for fine sand. This might be explained by the additional cohesion generated by the finer sand matrix.

In stage II, the breach widens by erosion and the width of the crest decreases until it vanished at $t = t_2$. Stage II occurs at $t_2 = 60$ s for coarse sand and $t_2 = 57$ s for fine sand. The inflow grows.

In stage III, the deepening and widening continues until the dike in the breach is washed out down to the base of the dike. Stage III appears to be a steady state in our experiment. It occurs at time $t = t_3 = 600$ s for both grain sizes.

One important difference between the two grain sizes is the impact of seepage. As observed in Figure 5, at the toe of the coarse sand dike, a flow is observed. This flow is due to the seepage through the dike and is not present in the fine sand dike (Figure 6). However, the main failure mechanism is still the overtopping over the dike through the breach. We will see in the next section that both sand types result in the same breach evolution process.

4.2. Evolution of the breach geometry

Figure 7a and b show the evolution of the dike along its centreline, in the direction of the flow. The process clearly shows similarities with the observations presented by Coleman et al. (2002, p. 833, figure 6) as a pivot point clearly appears at the downstream toe in both cases. Coleman characterizes this particular juncture as a pivot due to the continuous erosion that causes the dike to revolve around it over time. Unlike Coleman's observations, the pivot's position in both scenarios is consistently located beyond the initial construction of the dike toe. This occurrence is likely

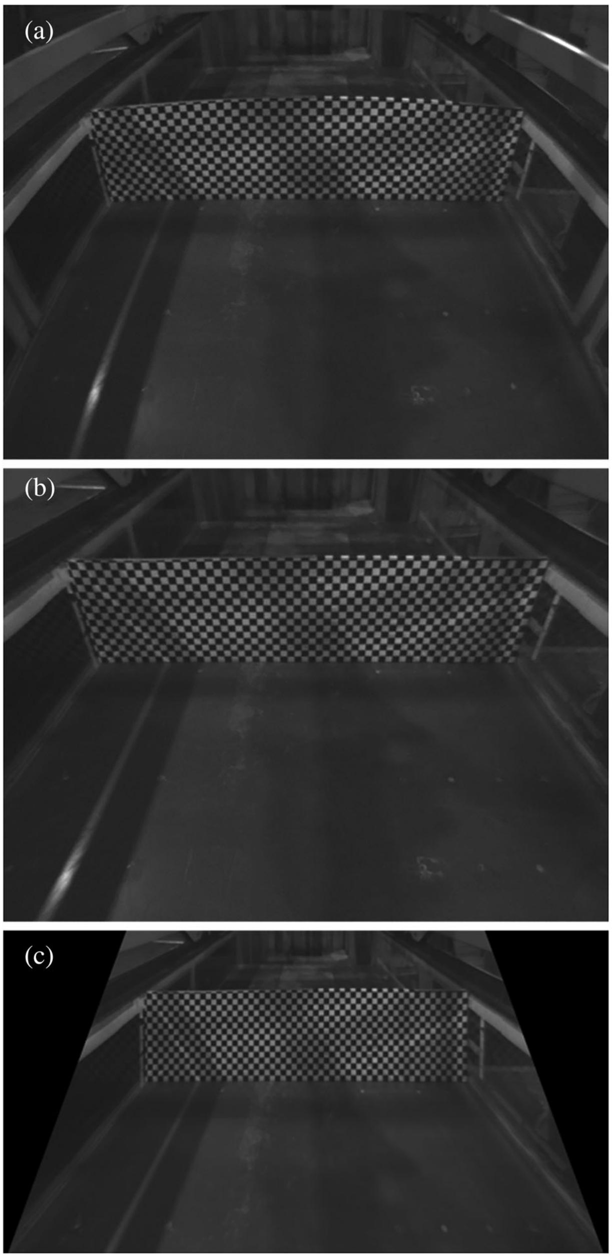

Figure 3. The initial acquired image (a) is subject to distortion. It is important to post-process the image. The figure shows the image after correction of the barrel effect (b) and the perspective distortion (c).

attributed to the presence of sand at the downstream toe of the dike, as previously described. The presence of an erodible sand layer downstream of the dike is however more representative of field situations. A final slope is obtained in both cases at around 600 s, corresponding to a steady state. The fine sand erosion ends up with an adverse slope but also with a steeper slope than the coarse sand dike.

Figure 7c shows the dike level evolution for the cross-section located at the dike crest ($x = 0.65$ m) but similar conclusions can be drawn when studying other cross-sections of the dike. For the first 15 s, the bed level increases. One hypothesis to explain this increase is that a mixture of water and sediment is flowing rather than clear water, and the exact bed elevation cannot be seen

Table 1. Cross-sections measurements starting from the upstream foot of the dike

Cross-section	Location	Trial
C1	0.60 m	A
C2	0.65 m	B
C3	0.70 m	C
C4	0.80 m	A
C5	0.90 m	B
C6	1.00 m	C
C7	1.10 m	A
C8	1.20 m	B
C9	1.30 m	C

by the laser. Another hypothesis, although less probable, could be the influence of optical distortion due to the free surface, whose depth is more important in the first steps of overtopping. After 15 s, the dike is eroded with a decreasing erosion rate. The coarse sand dike is initially eroded faster than the fine one. However, the fine sand dike then catches up this delay and they both stabilize at the same level.

Both dikes present similar behaviour to Visser's observations (1998) when considering the widening of the breach, for different cross-sections (Figure 8). During stage I, the channel width at the crest does not change much, however a narrow channel is dug on the downstream slope. This channel widens slower in the case of the fine sand dike, due to a more cohesive behaviour than the coarse sand one. Conversely, the vertical digging speed seems similar for both cases. Subsequently, in stage II and up to 120 s, the breach and the downstream channel undergo progressive widening and deepening, until the eroded width of the breach aligns with that of the downstream channel. Finally, between 120 s and 600 s, corresponding to stage III, the geometry changes much more slowly before reaching an equilibrium or steady state. It is interesting to notice that, except for the section in the downstream slope at 600 s for the fine sand, all cross-sections are symmetrical, which attests the good conditions and the repeatability of the experiments. Globally, the coarse sand dike presents a smoother evolution than the fine sand dike. This can be explained by an apparent cohesion in the fine sand that creates a burst behaviour: small blocks of fine sand sliding together.

4.3. Evolution of the water level and discharge

As mentioned in the introduction, it is of core interest to predict the measured discharge across the breach. The discharge is directly related to the collapse of the dike. It can be deduced from the input discharge ($Q_{in} = 4\,\mathrm{l\,s^{-1}}$) combined with the evolution of the water level in the reservoir (indeed, the discharge Q through the breach corresponds to the evolution of the water level z_w in the reservoir multiplied by the horizontal surface A_r of the reservoir, i.e. $Q = Q_{in} - A_r \frac{dz_w}{dt}$. This estimation does not consider the seepage that was observed in the coarse

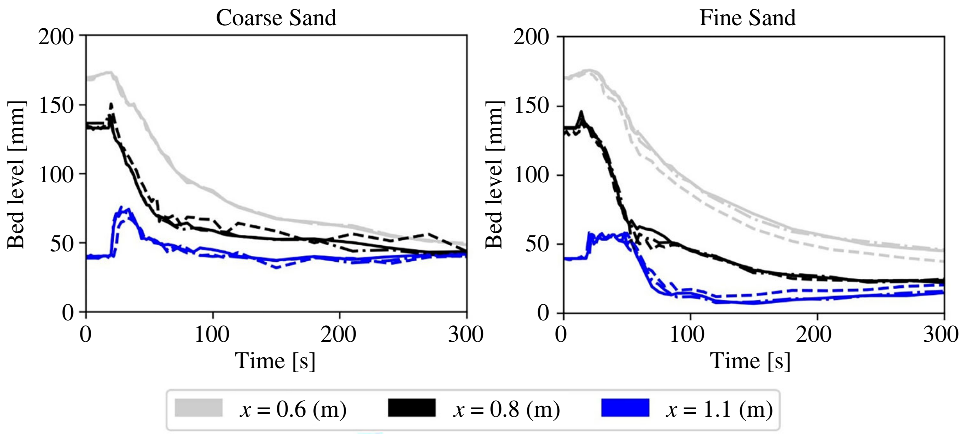

Figure 4. The repeatability of the protocol is assessed. The bed level evolution looks similar for three different trials (solid, dashed, dash-dotted) at three different positions (blue, grey and black) for both coarse and fine sand.

case, that is assumed to be negligible compared to the ongoing overtopping process.

Figure 9 illustrates the temporal evolution of (i) the water level captured by the ultrasonic probe G1 (Figure 1), and (ii) the temporal evolution of the discharge in the breach deduced from the measurements of the ultrasonic probe G1.

The water level in the reservoir is expected to grow until the collapse occurs. The peak of water level occurs around 41 s (coarse sand) and 46.5 s (fine sand) with a maximum level measured at.0.199 m (coarse sand) and 0.203 m (fine sand). The difference between the two sands can be explained by seepage through the dike for the coarse sand, and by an easier initial erosion due to a lower apparent cohesion. Conversely, the final water level ends up being higher for coarse sand than for fine sand: the final slope of the collapsed dike is steeper for fine sand (as shown in the profiles at Figure 7), which explains that the final water level will be lower. This also reflects the fact that coarse sand requires higher shear stresses to be eroded, when cohesion effects do not play any strengthening effect any more, as it is the case at the end of the experiment.

Accordingly, the water discharge is expected to evolve similarly to the water level. Indeed, the peak of water discharge is also delayed between coarse and fine sand. It occurs earlier for coarse sand (64 s) than for fine sand (67 s); their respective peak value is similar to the water level peak: less discharge for the coarse sand (0.009 m^3 s^{-1}) than for the fine sand (0.0096 m^3 s^{-1}). The delay between the highest water level and the highest discharge is approximately the same for both sand size, though (respectively 20.5 s and 23 s). After the peak, the slopes are very similar.

5. Numerical models

This section presents two numerical models: a simple unidimensional finite-volume model and a (more complex) bidimensional finite-volume model.

Both models are based on the shallow water equations (describing water mass and momentum conservation) augmented with the Exner equations (for sediment mass conservation). The equations are solved using an explicit finite-volume numerical scheme $U_i^{n+1} = \mathrm{f}(U_i^n, F^*)$, where the time is represented by the superscript n and the exchanges between volumes at the interfaces are represented by the fluxes F^*. After each temporal update, the bank stability conditions of the dike are verified. If the conditions are no more satisfied, a bank-failure operator is called to solve the collapse (Swartenbroekx et al., 2010). Then, a new time step can be run on a stabilized dike. The conserved values, the numerical schemes for fluxes estimation and the bank-failure operator will be explicitly defined for each model in the next subsections. Then, the models will be compared and validated against experimental data in Section 6.

5.1. One-dimensional model

The one-dimensional model considered here was developed by Franzini and Soares-Frazão (2018), based on the two-dimensional model of Murillo and García-Navarro (2010) and including a concept of "energy balance" as defined in Murillo and Garcia-Navarro (2014) or in Franzini and Soares-Frazão (2016).

In this model, the one-dimensional canal is divided into sections of small width. The flow is reduced to moving in only one direction (the axis of the flume) and the values of interest are described as averaged values over the considered cross-section (Figure 10). These values are the mass of water represented by the area of water A, the discharge Q, and the mass of sediments represented by the area A_b in the cross-section. These areas can evolve with time not only in depth but also in width, which permits the erosion of the dike to be captured.

More specifically, the water mass evolution only depends on the mass exchange at the cell boundaries,

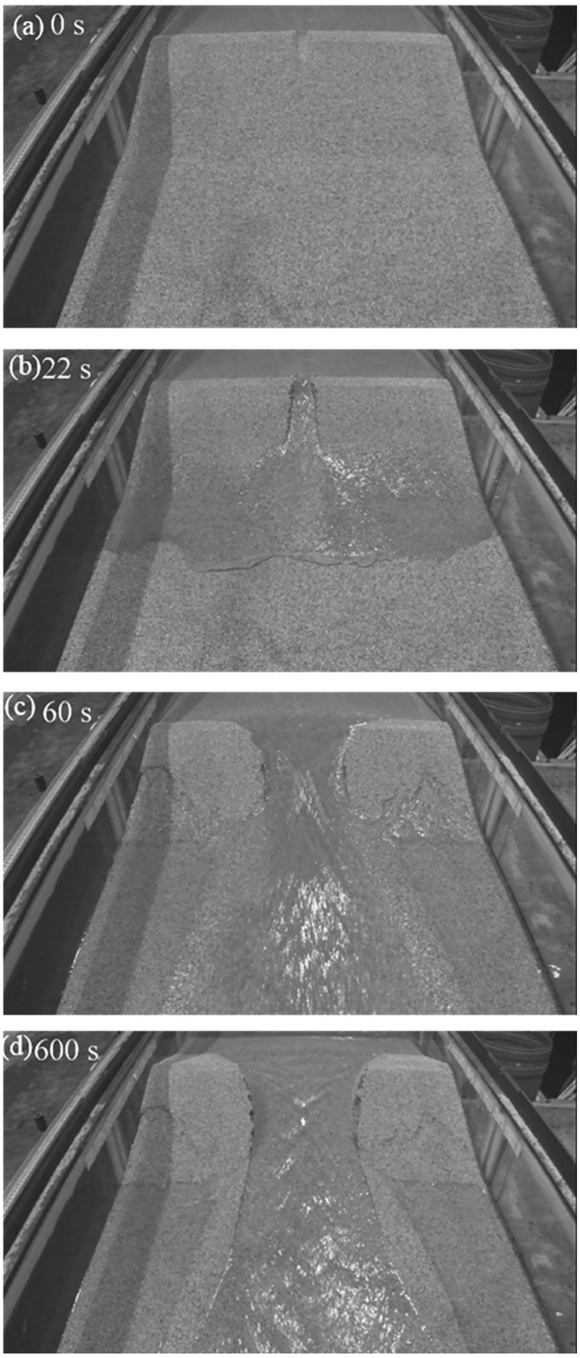

Figure 5. The failure evolution of the breach for coarse sand follows the three first stages of Visser (1998).

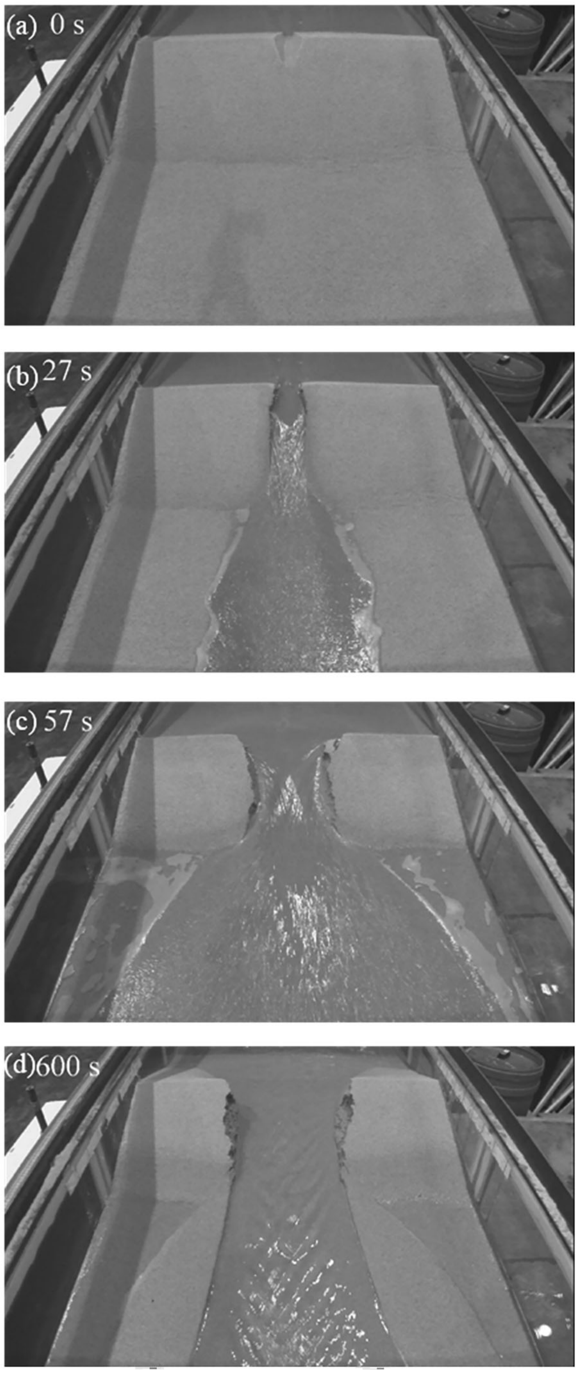

Figure 6. The failure evolution of the breach for fine sand follows the three first stages of Visser (1998).

just like the sediment transport. The closure equation required for the latter is the Meyer-Peter & Müller formula (1948), for which the range of application is mostly the non-cohesive particles moving with not much of suspension. The sediments discharge Q_s is hence:

$$Q_s = 8B\sqrt{g(s-1)d_{50}^3}\left(\frac{R\,S_f}{(s-1)d_{50}} - \theta_{cr}\right)^{1.5} \tag{1}$$

where s is the specific gravity of the sediments, d_{50} is the bed sediment median diameter, R is the hydraulic radius (defined as $R = A/P$), and θ_{cr} is the shear stress for initial sediment motion (here the value is set at 0.047).

The evolution of the discharge depends on hydrostatic pressure, the area of sediment evolution, the longitudinal component of lateral pressure (in case of expansion or constriction of the flume), and the friction slope. Together they define the exchange of momentum between adjacent cells that conduct the discharge evolution. Applying these constraints to the shallow-water equations, the temporal dynamics of the conserved variables $\boldsymbol{U} = [A, Q, A_b]^T$can be simplified under the

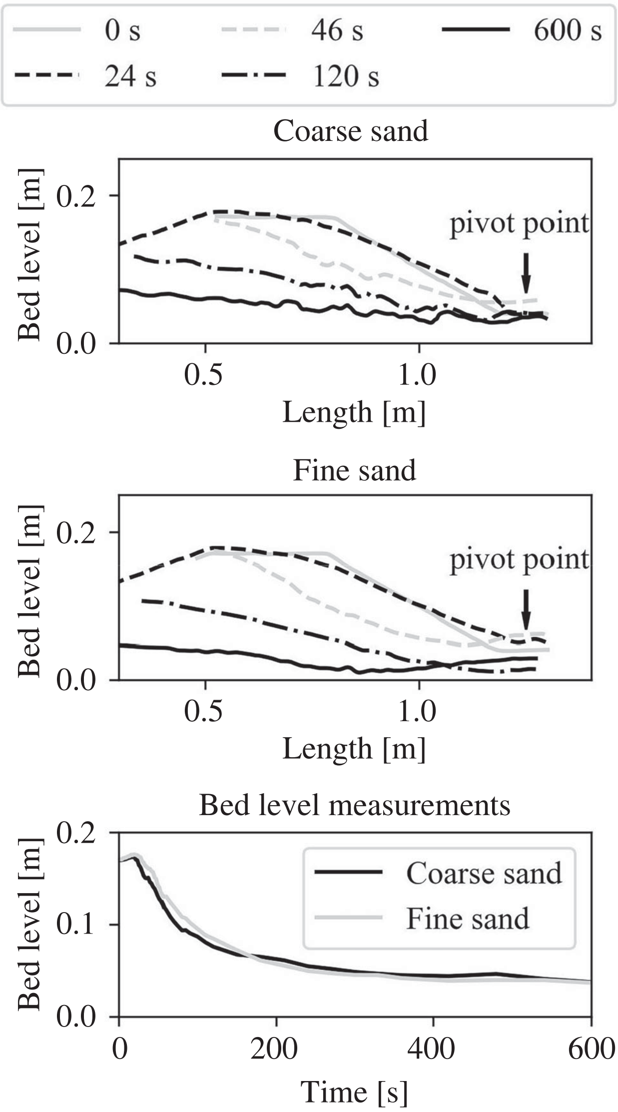

Figure 7. Validation of the theory of Coleman et al. (2002) Top: evolution of the bed level along the centreline of the flume: (a) coarse sand, (b) fine sand. Bottom: breach level evolution at the crest.

following equation in vector form:

$$\frac{\partial \boldsymbol{U}}{\partial \boldsymbol{t}}+\frac{\partial \boldsymbol{F}}{\partial \boldsymbol{x}}+\mathbf{H}\frac{\partial \boldsymbol{U}}{\partial \boldsymbol{x}}=\boldsymbol{S} \tag{2}$$

where $\boldsymbol{F}$ groups the momentum fluxes and hydrostatic pressure contributions:

$$\boldsymbol{F}=\begin{bmatrix} Q \\ \frac{Q^2}{A}+gI_1 \\ \frac{Q_s}{1-\varepsilon_0} \end{bmatrix} \tag{3}$$

where Q is the discharge, A is the area of water, $gI_1$is the hydrostatic pressure, Q_s the sediment discharge and ε_0 the sediment's porosity. $\boldsymbol{H}\,\partial \boldsymbol{U}/\partial x$ captures the impact of the morphological variation on the momentum, where $\mathbf{H}$ is the following matrix:

$$\mathbf{H}=\begin{bmatrix} 0 & 0 & 0 \\ 0 & 0 & \frac{gA}{B_s} \\ 0 & 0 & 0 \end{bmatrix} \tag{4}$$

B_s is the ratio to determine the discretization of the area of sediment evolution as $\Delta z_b = \Delta A_b/B_s$ (here equal to A/h, Figure 11). $\boldsymbol{S}$ are the source terms (lateral pressure and friction):

$$\boldsymbol{S}=\begin{bmatrix} 0 \\ gI_2-gAS_f \\ 0 \end{bmatrix} \tag{5}$$

For a rigorous definition of the matrices $\boldsymbol{U}$, $\boldsymbol{F}$, $\boldsymbol{H}$ and $\boldsymbol{S}$, as well as a more complete explanation of the model, we refer the reader to Franzini and Soares-Frazão (2018).

Equation (2) is numerically solved via a finite volume scheme applied to this 1D formulation over computational cells of length dx centred on each cross-section. Then the (temporal) explicit resolution scheme is given by:

$$\boldsymbol{U}_i^{n+1}=\boldsymbol{U}_i^n-\frac{\Delta t}{\Delta x}\left(\boldsymbol{F}_{i+1/2}^{*L}-\boldsymbol{F}_{i-1/2}^{*R}\right) \tag{6}$$

where the fluxes $\boldsymbol{F}_{i-1/2}^{*R}$ and $\boldsymbol{F}_{i+1/2}^{*L}$ are the lateralized contributions, respectively from the upstream and downstream sections calculated using the augmented Roe scheme with energy balance (Franzini & Soares-Frazão, 2018). The source terms (topography and friction) are directly integrated to the fluxes yielding lateralized values (i.e. values that are different for the left and right cells, the difference being the result of the source term).

The area of erosion/deposition, A_b, is distributed along the section proportionally to the local water depth resulting in a non-uniform erosion of the cross-section. No erosion occurs if the water depth is equal to zero. The classical sediment transport theory links the shear stress at the bottom of the flow to the water depth. Therefore, linking the sediment transport to the water depth distribution along the section seems to be a reasonable assumption.

Last but not least, a tilting bank failure operator is also included. It is activated after each time step if the stability conditions are not satisfied anymore (with respect to the dry and wet critical friction angles given in Section 2). The general operation of the process is illustrated on Figure 11: section BC is initially steeper than the friction angle, therefore it is unstable and is tilted to its stability angle. Segment B'C' is now stable, but segment AB' is now unstable and will be tilted in the next operation. Unlike in Franzini and Soares-Frazão (2018), the failure operator is here used both transversally and longitudinally to improve the capture of sediment mass failures that occur in both directions.

5.2. Two-dimensional model

The 2D finite-volume model solves the shallow water and Exner equations on unstructured triangular meshes.

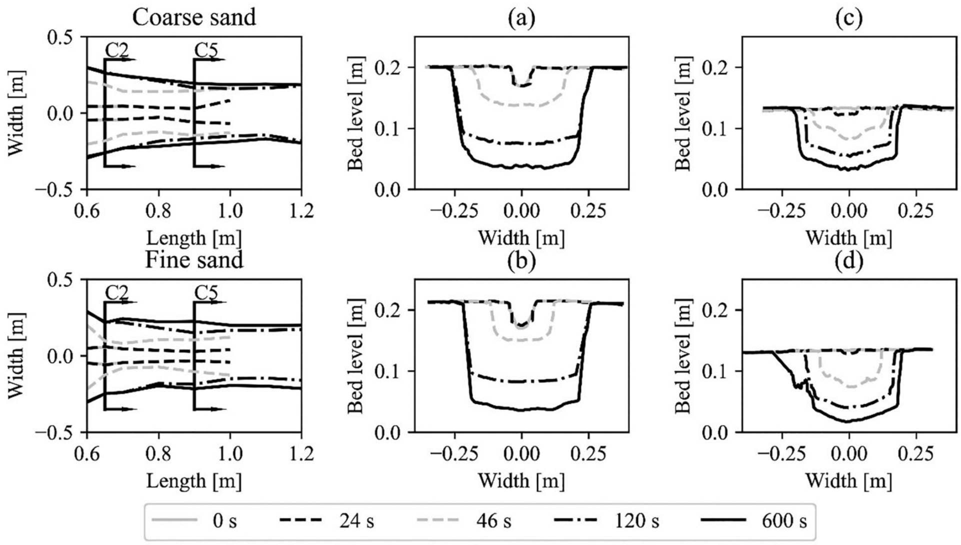

Figure 8. Evolution of the width of the breach (left) along time (experiments) and of two cross-sections: at the crest ($x = 0.65$ m, laser-sheet C2) with coarse sand (a) and with fine sand (b); and in the slope ($x = 0.9$ m, laser-sheet C5) with coarse sand (c) and fine sand (d). The stages identified in Visser's theory also appear here.

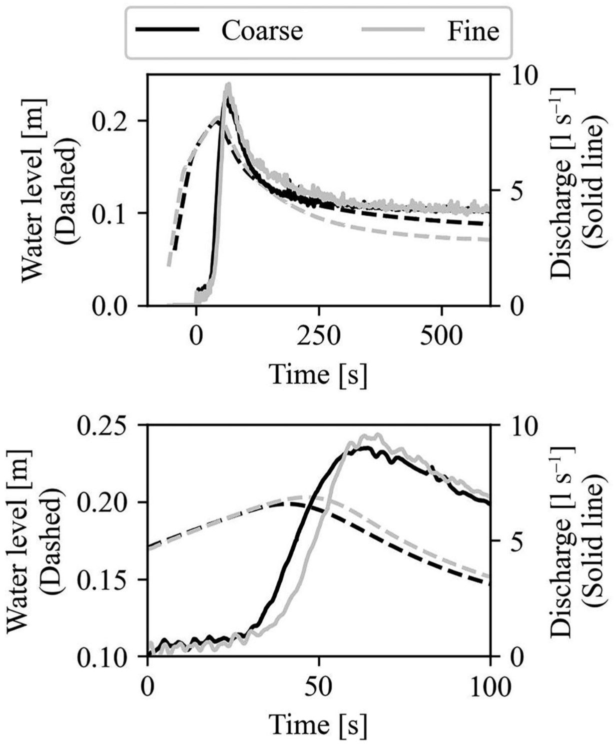

Figure 9. Evolution of the reservoir water level (from gauge G1, dashed line) and of the water discharge (solid line). The figure below is a zoom between 0 s and 100 s of the figure above.

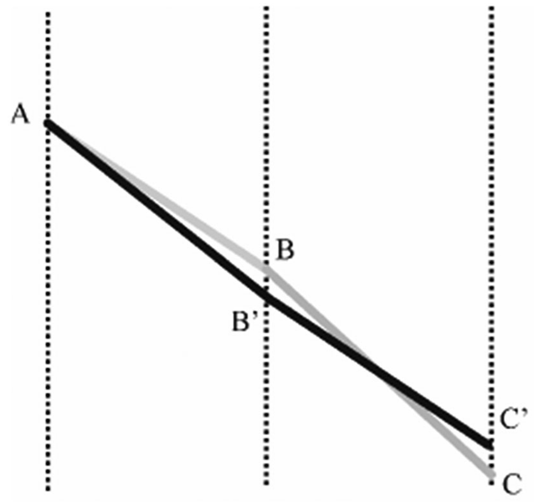

Figure 10. Bank failure operator (Franzini et al, 2018).

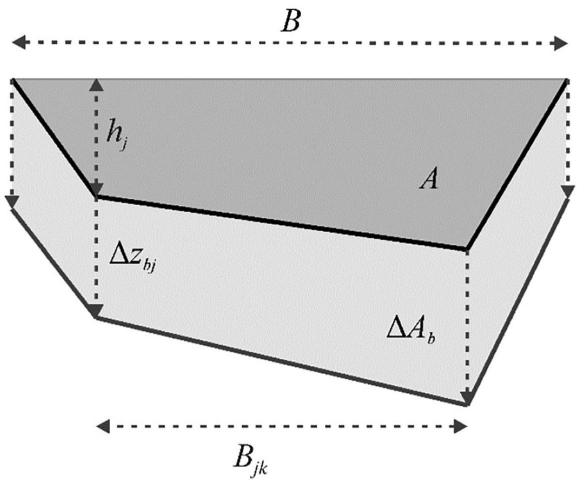

Figure 11. Discretization of the erosion.

The flow is now free to move in two directions and the fluxes are evaluated using a modified LHLLC scheme (Soares Frazao & Zech, 2011). Like in the unidimensional model, the sediment transports are also computed using the Meyer-Peter and Müller (1948) formula (1).

The conserved variables are now the water depth h, the discharge q_x in the direction of the flow and q_y in the flat perpendicular direction, and the sediments level z_b, i.e. $\boldsymbol{U} = [h, q_x, q_y, z_b]^T$. The temporal dynamics can be described in vector form as:

$$\frac{\partial \boldsymbol{U}}{\partial t} + \frac{\partial \boldsymbol{F}}{\partial x} + \frac{\partial \boldsymbol{G}}{\partial y} = \boldsymbol{S} \tag{7}$$

$$\boldsymbol{F} = \begin{bmatrix} uh \\ u^2h + gh^2/2 \\ uvh \\ q_{sx}/(1-e_0) \end{bmatrix} \tag{8}$$

$$\boldsymbol{G} = \begin{bmatrix} vh \\ uvh \\ v^2h + gh^2/2 \\ q_{sy}/(1-\varepsilon_0) \end{bmatrix} \tag{9}$$

$$\boldsymbol{S} = \begin{bmatrix} 0 \\ gh\left(-\frac{\partial z_b}{\partial x} - S_{fx}\right) \\ gh\left(-\frac{\partial z_b}{\partial y} - S_{fy}\right) \\ 0 \end{bmatrix} \tag{10}$$

where vectors $\boldsymbol{F}$ and $\boldsymbol{G}$ group the momentum fluxes and hydrostatic pressure contributions and variation in the x-axis and y-axis directions respectively, also considering transverse fluxes; $\boldsymbol{S}$ are the source terms considering slope and friction effects; u is the velocity component along the x-axis; v the velocity component along the y-axis; z_b the bed level; q_{sx} the sediment transport along the x-axis; q_{sy} the sediment transport along the y-axis; S_{fx} and S_{fy} the friction slope along the x-axis and the y-axis, respectively.

The finite-volume scheme to numerically solve Equation (4) is as follows:

$$\boldsymbol{U}_i^{n+1} = \boldsymbol{U}_i^n - \frac{\Delta t}{\Omega_i} \sum_{j=1}^{3} \mathbf{R}_j^{-1} \overline{\boldsymbol{F}^*} L_j + \mathbf{S}_i \Delta t \tag{11}$$

where Ω_i is the cell area and L_j is the interface length; the fluxes at the interfaces $\overline{\boldsymbol{F}^*}$ are represented considering normal and tangential directions obtained through the rotation matrix $\mathbf{R}$ to be expressed in a local coordinates system attached to the interface, and whose components are computed from the neighbouring cells using the LHLLC scheme (Soares Frazao & Zech, 2011).

When the local slope of a cell increases excessively, the failure of the bank is simulated by a bank-failure operator (Swartenbroekx et al., 2010) activated under the same conditions as in the unidimensional model. As the slope of a cell exceeds the considered angle of repose, the algorithm is used to distribute the slope of adjacent cells and check their proper balance.

6. Discussion of the numerical simulations and the experiments

In this section, the aforementioned models will be compared to experimental data. The 1D-mesh is composed of 363 cells, evenly distributed along the channel. The 2D-mesh is composed of approximately 200,000 elements with the smallest ones located at the crest of the dike with an average edge length of 2.5 mm. Such a refined mesh is needed to capture the widening of the breach better as it has a tremendous impact on the bank failure operator. The codes are developed in C++ and the 2D code is parallelized with OpenMP. A substantial difference between the two models lies in the computational time and the computational resources needed to obtain a prediction. It is clear that running a 1D-model on hundreds of cells is faster and less consuming than running a 2D-model on hundreds of thousands of cells. While the 1D model took less than an hour to simulate the failure, the 2D models took several days. This difference of computation time is balanced by the amount of data that we can retrieve from each model. While the 1D model is only able to provide information regarding the discharge and the area at a particular x-position, the 2D model can provide precise information regarding the (e.g.) velocities at very local scale, in the x–y directions. Even if the erosion process is mostly active in the flow direction, taking the y-direction processes into account is an asset for the 2D model when evaluating the breach lateral evolution. The precise knowledge of the water depth, directly linked to the shear stress, in the full area is also of utmost importance when looking for an optimal design for a given dike. Considering these points, we expect the 2D model to perform better than the 1D model for predicting the dike breaching process. The state of the flow is captured at $t_0 = 0$ s, $t_1 = 46$ s, and $t_2 = 120$ s.

6.1. Comparison with the one-dimensional model

Figures 12–14 show the results obtained using the unidimensional model to simulate the dike breaching with coarse and fine sand. Figures are presented in similar way to Section 4 to ease the comparison by the reader: results in Figures 13 and 14 can confirm the theory of Visser (1998) and Coleman et al. (2002). For comparison purposes, Figure 14 illustrates the water level and discharge evolution over time.

Once again, one can observe that the failure process can be divided into three parts: (i) the first 50 s (illustrated here by the results at 46 s), (ii) between 50 and 120 s (illustrated here by the results at 120 s), and (iii) between 120 s and 600 s. The 1D model is able to capture the widening and deepening of the breach during the first phase as observed in Figure 12 (the solid lines represent the results at 46 s). This phase ends approximately at the peak of the measured outflow discharge, that occurs after the peak water-level in the reservoir (Figure 14).

During the second phase, after the maximum water level has been reached in the reservoir, erosion accelerates, resulting in an increase of the breached section

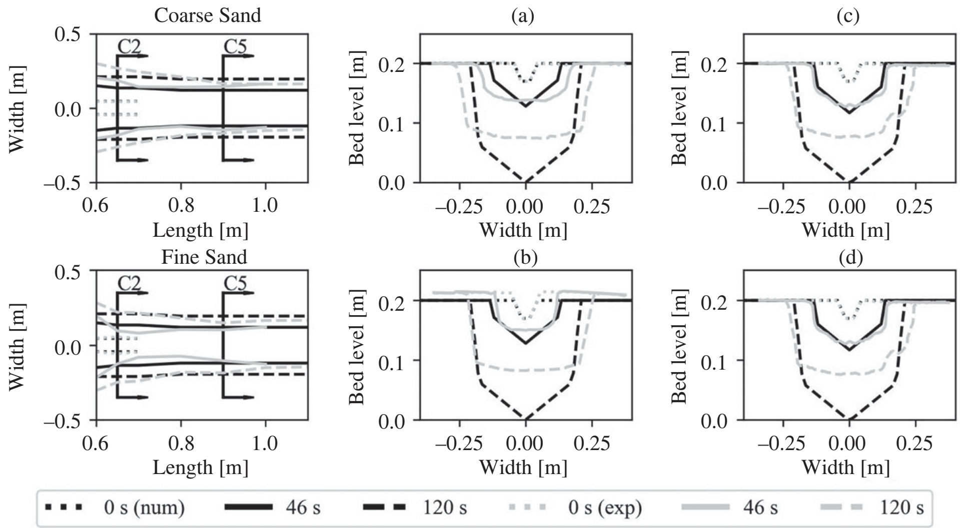

Figure 12. Evolution of the width of the breach (left) along time (1D model) and of two cross-sections: at the crest ($x = 0.65$ m, laser-sheet C2) with coarse sand (a) and with fine sand (b); and in the slope ($x = 0.9$ m, laser-sheet C5) with coarse sand (c) and fine sand (d). The 1D predictive model (black) captures well the widening of the breach but fails at estimating its depth. Experimental results are presented in grey.

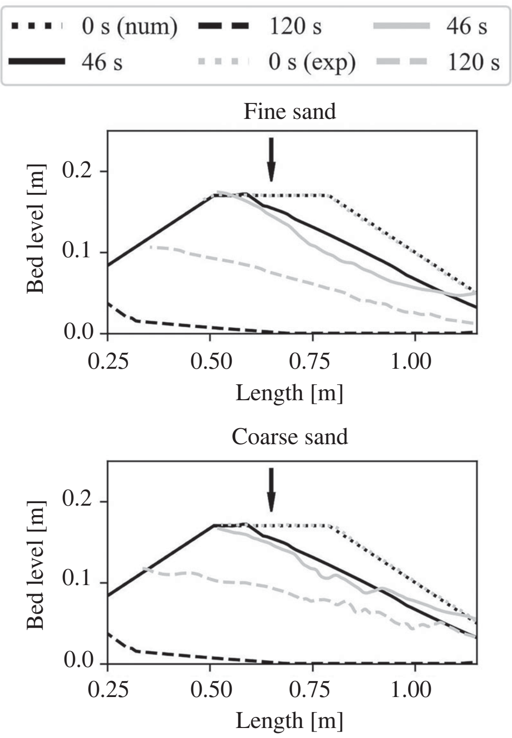

Figure 13. Evolution of the bed level along the centreline of the flume (1D model) for coarse sand (above) and fine sand (below). As the time lasts, the numerical results (black) differ more and more from experiments (grey) because the 1D model fails at predicting the digging of the flow.

and consequently a decrease in the water level in the reservoir as the inflow discharge is not sufficient any more to maintain the level constant (Figures 12 and 13). The erosion process computed in the 1D model is overestimated, leading to an overestimation of the peak discharge and a lower water level in the reservoir. The computed erosion is such that it ends up reaching the fixed bottom of the channel. Consequently, the computed peak discharge at the breach is much higher than the experimental one because of the faster erosion of the breach, but ends up at almost the same rate. In contrast, the widening is well estimated even if the breach banks are steeper than the real ones.

It can also be observed that the cross-sections present a triangular shape in the simulation but not in the experiment. This difference in shape is created by the bank failure operator: the tilting of the bank is so important that both banks meet in the middle of the breach. Later, the non-uniform erosion increases this triangular shape, as the erosion is higher in deeper water.

To sum up, the unidimensional model fails at predicting the erosion of the dike in that it overestimates the peak outflow discharge and the erosion depth. However, the prediction of the widening of the breach is satisfying. We can therefore consider that one-dimensional model is useful when being used as first approach for the design of breach-induced floods.

6.2. Comparison with the two-dimensional model

Figures 15–17 show the results obtained using the two-dimensional simulation.

Similarly to the one-dimensional case, the failure process can be divided into three parts corresponding to the stages previously described: (i) the first 50 s (illustrated here by the results at 46 s), (ii) between 50 and 120 s (illustrated here by the results at 120 s), and (iii) between 120 s and 600 s. This model gives a good prediction of the overall evolution of the breach. The evolution of the bottom profile is relatively close to what has been observed during the experiment. In

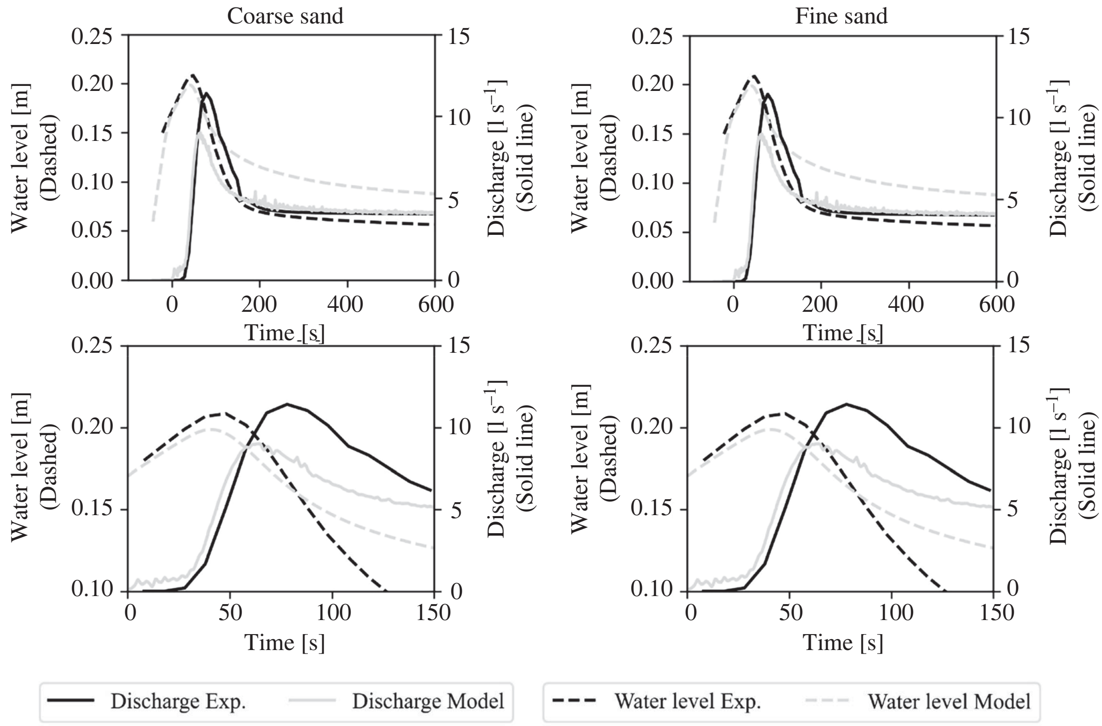

Figure 14. Evolution (1D model) of the water level in the reservoir (dashed lines) and discharge in the breach (solid lines) for coarse sand (left) and fine sand (right). The model (black) detects the peak correctly but fails at estimating its actual value (grey). The graphs below are a zoom of the graphs above.

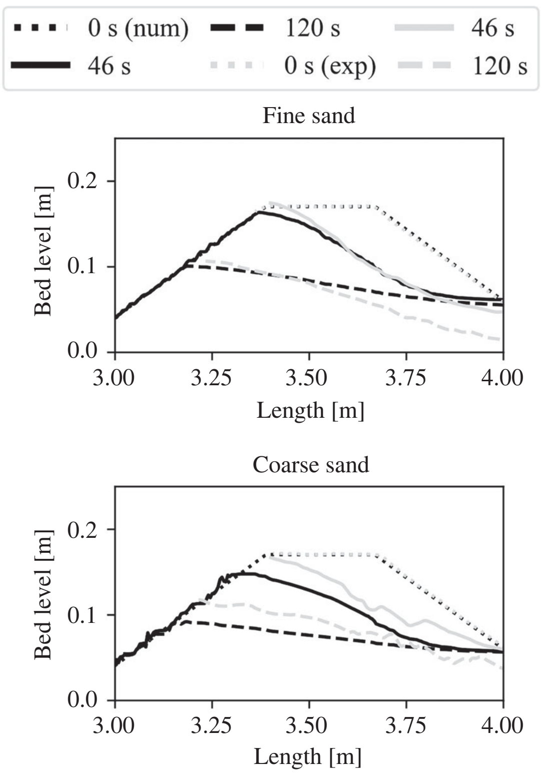

Figure 15. Evolution of the bed level along the centreline of the flume (2D model) for coarse sand (above) and fine sand (below). Compared to Figure 12, the numerical results (black) capture better the deepening of the sand level measured by experiments (grey).

general, Visser's (1998) prediction is well reproduced: during the first phase, the model estimates correctly the widening of the breach although the model yields less symmetrical results than the observed ones (Figure 15). This could be attributed to the bank failure operator that is activated every 50 time steps. Indeed, it was shown in Swartenbroekx et al. (2010) that a converged solution can be obtained with the bank failure operator, but at higher computational costs. Therefore, the authors recommended to apply it for a limited number of iterations within each time step, yielding satisfactory but slightly less accurate results.

During the second phase, the breach widens more than in the reality. However, the breach level evolution is correctly captured (Figure 16), as theorised by Coleman et al. (2002), and the model is able to predict the breach shape with the local constriction.

The discharge and reservoir water level are also well predicted (Figure 17) despite a slight overestimation of the peak of discharge. This overestimation explains that the model widens the breach too fast.

Finally, Figure 18 compares the results obtained with 1D and 2D models. It can be observed that the 1D model is not able to capture the breach constriction. This is not surprising since no lateral forces are really applied on the banks, in the 1D model. This confirms the importance of the y-direction flow in the erosive process, as explained previously. However, the width at the crest (after 0.6 m) is well predicted in both cases.

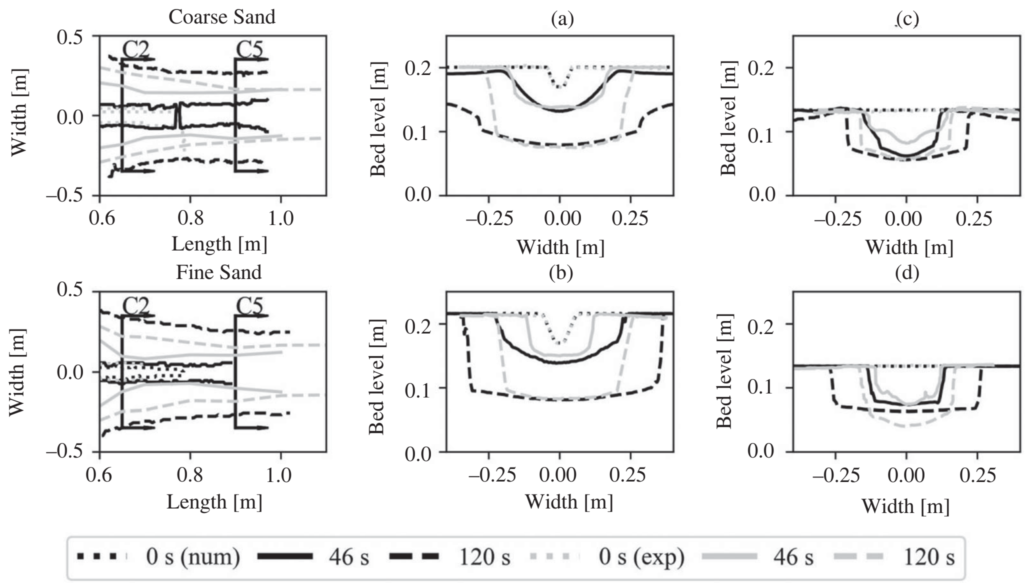

Figure 16. Evolution of the width of the breach (left) along time (2D model) and of two cross-section: at the crest ($x = 0.65$ m, laser-sheet C2) with coarse sand (a) and with fine sand (b); and in the slope ($x = 0.9$ m, laser-sheet C5) with coarse sand (c) and fine sand (d). The 2D predictive model (black) captures well the depth of the breach but fails at estimating its width, which is the opposite than the 1D model (Figure 11). Experimental results are presented in grey.

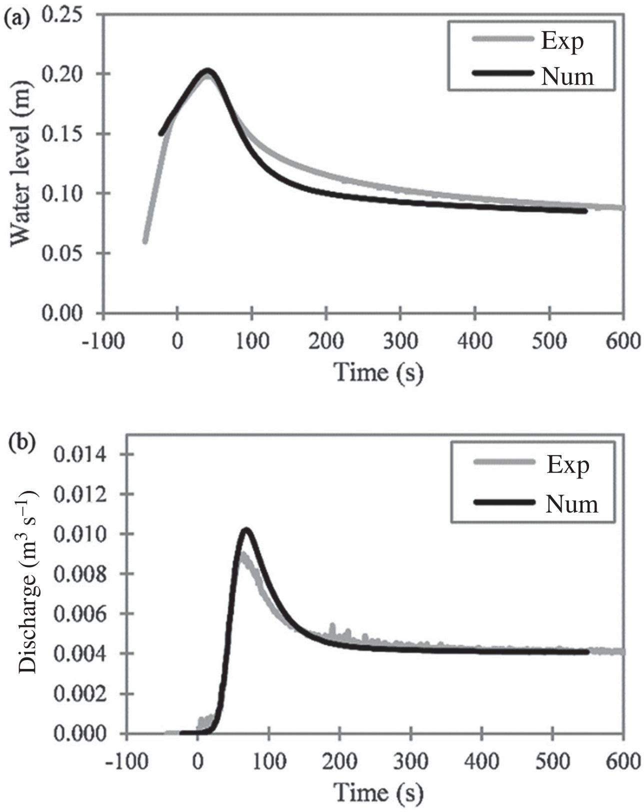

Figure 17. Evolution of (a) the water level in the reservoir and (b) the discharge in the breach for coarse sand as calculated using the 2D model.

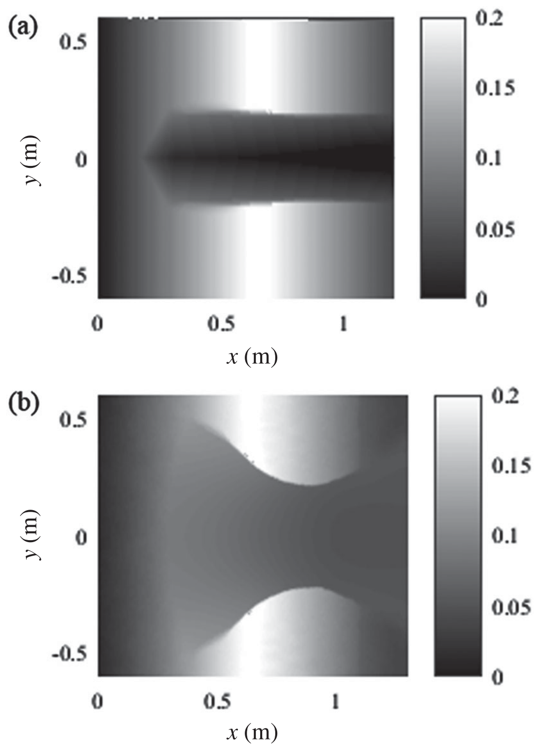

Figure 18. Comparison of the breach geometry after 120 s. The colour bar represents the bed level, for (a) the 1D model and (b) the 2D model.

7. Conclusions

Small-scale experiments of dike breaching have been performed using fine and coarse grain sizes. The overall process demonstrated strong consistency with traditional observations found in the literature regarding the widening and deepening of breach in non-cohesive fill dikes (Coleman et al., 2002; Visser, 1998).

First, the fine sand showed an apparent cohesion leading to steep slopes, block mass failure and therefore irregular widening of the breach. Conversely, the width variation was much smoother for the coarse sand dike. Second, the fine sand dike failure exhibits a higher and later peak for both the water level in the upstream reservoir and the breach discharge. It was also observed that the delay between the reservoir level peak and the peak discharge were similar for both sand sizes.

Then, the experimental results have been compared to numerical simulations using 2D and 1D models. Despite its simplicity, the simple 1D model showed good results for the initial stage of the dike failure for all the monitored parameters even though the width evolution along the breach was straighter than the experiment. However, the results after the peak discharge were not as good, as the 1D model tends to overestimate the erosion rate. Nevertheless, the width evolution along the breach was correctly estimated even if presenting bank slopes that were too straight. However, the model was not able to fully evaluate the evolution of the dike in all directions. The fact that the 1D model needs less computational cost and still provides interesting results for the breach width makes it very useful to determine a first order of magnitude for failure time and discharge in initial stages of design. For further work, it would be interesting to study other ways to distribute the erosion across a transversal section, see for instance Martínez-Aranda et al. (2019).

The 2D model showed good results in predicting the overall evolution of the dike breach. The model was more accurate than the 1D model in predicting the peak discharge and water level peak, which are ultimately the quantities of interest.

The results presented here show the ability of the models to complement each other to get closer to reality. However, it should be kept in mind that these models, as well as most of the models in the literature, are limited to the evaluation of breaches in dikes made of non-cohesive materials. In the future, efforts must be undertaken to develop numerical models capable of reproducing cohesive effects, due to water content or to the nature of the materials themselves, through a more sophisticated consideration of mechanics. The aim is to be able to assess the resistance to overtopping flows of real dikes, more often made of cohesive materials.

Acknowledgements

The authors would like to thank Charles Descantons and Rémy Dujardin (2014) for their help in designing and running the experiments.

Data availability statement

The dataset is publicly available in the following repository: https://doi.org/10.14428/DVN/R7VH3G

Disclosure statement

No potential conflict of interest was reported by the author(s).

Notation

A	area of water (m^2)
A_r	planar area of the reservoir (m^2)
A_b	area of sediments (m^2)
d_{50}	median sediment diameter (mm)
$\boldsymbol{F}, \boldsymbol{F}^*$	vector of fluxes
G_i	measurement gauge
$\mathbf{G}$	fluxes in the y-direction
$\mathbf{H}$	alternative flux matrix
h	water depth (m)
Q	water discharge (m^{3}s^{-1}), water discharge per metre (m^{2}s^{-1})
q_x, q_y	water discharge per unit width in the x- and y-directions (m^{3}s^{-1})
Q_s	sediment transport (m^{3}s^{-1}), sediment transport per metre (m^{2}s^{-1})
q_{sx}, q_{sy}	sediment discharge per unit width in the x- and y-directions (m^{2}s^{-1}).
R	hydraulic radius (m)
$\mathbf{R}$	rotation matrix
$\mathbf{S}$	vector of source terms
s	specific gravity of the sediments (−)
S_f	friction slope (−)
T, t_i	time (s)
$\boldsymbol{U}$	vector of conserved variables
$\boldsymbol{U}_i^n$	conserved variables in the element i at time step n
u	velocity component along the x-axis
v	velocity component along the y-axis
x	direction of the flume
y	direction of the width of the flume
z	depth direction
z_b	bed level (m)
z_w	water level (m)
ϵ_0	bed porosity (−)
θ_{cr}	critical shear stress (−)
Ω	cell area (m^2)

ORCID

Sandra Soares-Frazao http://orcid.org/0000-0001-5088-0278

References

ASCE/EWRI Task Committee on Dam/Levee Breaching. (2011). Earthen embankment breaching. *Journal of Hydraulic Engineering 137*(12), 1549–1564.

Barzgaran, M., Mahdizadeh, H., & Sharifi, S. (2019). Numerical simulation of bedload sediment transport with the ability to model wet/dry interfaces using an augmented Riemann solver. *Journal of Hydroinformatics 21*(5), 834–850. https://doi.org/10.2166/hydro.2019.046

Coleman, S. E., Andrews, D. P., & Webby, M. G. (2002). Overtopping breaching of noncohesive homogeneous embankments. *Journal of Hydraulic Engineering*, *128*(9), 829–838.

Delpierre, N., Rattez, H., & Soares-Frazao, S. (2023). Finite-volume coupled surface-subsurface flow modelling in earth dikes. *Journal of Hydraulic Research*, *61*(5), 754–763. https://doi.org/10.1080/00221686.2023.2246936

Foster, M., Fell, R., & Spannagle, M. (2000). The statistics of embankment dam failures and accidents. *Canadian Geotechnical Journal*, *37*(5), 1000–1024. https://doi.org/10.1139/t00-030

Franzini, F., & Soares-Frazão, S. (2016). Efficiency and accuracy of lateralized HLL, HLLS and augmented roe's scheme with energy balance for river flows in irregular channels. *Applied Mathematical Modelling*, *40*(17), 7427–7446. https://doi.org/10.1016/j.apm.2016.02.007

Franzini, F., & Soares-Frazão, S. (2018). Coupled finite-volume scheme with adapted augmented Roe scheme for simulating morphological evolution in arbitrary cross-sections. *Journal of Hydroinformatics*, *20*(5), jh2018109. https://doi.org/10.2166/hydro.2018.109

Juez, C., Murillo, J., & García-Navarro, P. (2014). A 2D weakly-coupled and efficient numerical model for transient shallow flow and movable bed. *Advances in Water Resources 71*, 93–109. https://doi.org/10.1016/j.advwatres.2014.05.014

Martínez-Aranda, S., Fernández-Pato, J., & García-Navarro, P. (2023). Non-Equilibrium bedload transport model applied to erosive overtopping dambreach. *Water*, *15*(17), 17. https://doi.org/10.3390/w15173094

Martínez-Aranda, S., Meurice, R., Soares-Frazão, S., & García-Navarro, P. (2021). Comparative analysis of HLLC- and roe-based models for the simulation of a Dam-break flow in an erodible channel with a 90○ bend. *Water*, *13*(13), 13. https://doi.org/10.3390/w13131840

Martínez-Aranda, S., Murillo, J., & García-Navarro, P. (2019). A 1D numerical model for the simulation of unsteady and highly erosive flows in rivers. *Computers & Fluids*, *181*, 8–34. https://doi.org/10.1016/j.compfluid.2019.01.011

Meurice, R., & Soares-Frazão, S. (2020). A 2D HLL-based weakly coupled model for transient flows on mobile beds. *Journal of Hydroinformatics* 22(5), 1351–1369. https://doi.org/10.2166/hydro.2020.033

Meyer-Peter, E., & Müller, R. (1948). *Formulas for Bed-Load transport*. *3*, 39–64.

Morris, M., Hassan, M., Kortenhaus, A., & Visser, P. (2009). Breaching Processes: A state of the art review. *FLOOD site Project Report, T06-06-03*.

Murillo, J., & Garcia-Navarro, P. (2014). Accurate numerical modeling of 1D flow in channels with arbitrary shape. Application of the energy balanced property. *Journal of Computational Physics*, *260*, 222–248. https://doi.org/10.1016/j.jcp.2013.12.040

Murillo, J., & García-Navarro, P. (2010). An exner-based coupled model for two-dimensional transient flow over erodible bed. *Journal of Computational Physics*, *229*(23), 8704–8732. https://doi.org/10.1016/j.jcp.2010.08.006

Müller, C., Frank, P.-J., & Hager, W. (2016). Dyke overtopping: effects of shape and headwater elevation. *Journal of Hydraulic Research*, *54*(4), 1–13. https://doi.org/10.1080/00221686.2016.1170072

Pan, Y., Li, L., Amini, F., & Kuang, C. (2015). Overtopping erosion and failure mechanism of earthen levee strengthened by vegetated HPTRM system. *Ocean Engineering*, *96*, 139–148. https://doi.org/10.1016/j.oceaneng.2014.12.012

Schmocker, L., Frank, P.-J., & Hager, W. (2014). Overtopping dike-breach: effect of grain size distribution. *Journal of Hydraulic Research*, *52*(4), 559–564. https://doi.org/10.1080/00221686.2013.878403

Schmocker, L., & Hager, W. H. (2012). Plane dike-breach due to overtopping: effects of sediment, dike height and discharge.. *Journal of Hydraulic Research*, *50*(6), 576–586. https://doi.org/10.1080/00221686.2012.713034

Sills, G. L., Vroman, N. D., Wahl, R. E., & Schwanz, N. T. (2008). Overview of New Orleans levee failures: lessons learned and their impact on national levee design and assessment. *Journal of Geotechnical and Geoenvironmental Engineering*, *134*(5), 556–565. https://doi.org/10.1061/(ASCE)1090-0241(2008)134:5(556)

Soares Frazao, S., & Zech, Y. (2011). HLLC scheme with novel wave-speed estimators appropriate for two-dimensional shallow-water flow on erodible bed. *International Journal for Numerical Methods in Fluids*, *66*(9), 1019. https://doi.org/10.1002/fld.2300

Soares-Frazão, S., Le Grelle, N., Spinewine, B., & Zech, Y. (2007). Dam-break induced morphological changes in a channel with uniform sediments: measurements by a laser-sheet imaging technique. *Journal of Hydraulic Research*, *45*(sup1), 87–95. https://doi.org/10.1080/00221686.2007.9521835

Swartenbroekx, C., Soares-Frazão, S., Staquet, R., & Zech, Y. (2010). Two-dimensional operator for bank failures induced by water-level rise in dam-break flows. *Journal of Hydraulic Research*, *48*(3), 302–314. https://doi.org/10.1080/00221686.2010.481856

Van Emelen, S., Zech, Y., & Soares-Frazão, S. (2015). Impact of sediment transport formulations on breaching modelling. *Journal of Hydraulic Research*, *53*(1), 60–72. https://doi.org/10.1080/00221686.2014.939111

Visser, P. J. (1998). *Breach growth in sand-dikes*. https://repository.tudelft.nl/islandora/object/uuid%3A3721e23b-d34c-45a9-8b36-e5930462d8e2.

Wu, W., Marsooli, R., & He, Z. (2012). Depth-averaged two-dimensional model of unsteady flow and sediment transport due to noncohesive embankment break/breaching. *Journal of Hydraulic Engineering 138*(6), 503–516. https://doi.org/10.1061/(ASCE)HY.1943-7900.0000546

Zhang, Y., Chen, G., Hu, J., Chen, X., Yang, W., Tao, A., & Zheng, J. (2017). Experimental study on mechanism of sea-dike failure due to wave overtopping. *Applied Ocean Research*, *68*, 171–181. https://doi.org/10.1016/j.apor.2017.08.009

Zhou, G. G. D., Zhou, M., Shrestha, M. S., Song, D., Choi, C. E., Cui, K. F. E., Peng, M., Shi, Z., Zhu, X., & Chen, H. (2019). Experimental investigation on the longitudinal evolution of landslide dam breaching and outburst floods. *Geomorphology*, *334*, 29–43. https://doi.org/10.1016/j.geomorph.2019.02.035